

# A predictive model for high-frequency operation of two-dimensional transistors from first-principles

Cite as: J. Appl. Phys. **128**, 234502 (2020); <https://doi.org/10.1063/5.0030633>

Submitted: 23 September 2020 . Accepted: 02 December 2020 . Published Online: 17 December 2020

 Biswapriyo Das, and  Santanu Mahapatra



View Online



Export Citation



CrossMark



## Your Qubits. Measured.

Meet the next generation of quantum analyzers

- Readout for up to 64 qubits
- Operation at up to 8.5 GHz, mixer-calibration-free
- Signal optimization with minimal latency

Find out more



# A predictive model for high-frequency operation of two-dimensional transistors from first-principles

Cite as: J. Appl. Phys. 128, 234502 (2020); doi: 10.1063/5.0030633

Submitted: 23 September 2020 · Accepted: 2 December 2020 ·

Published Online: 17 December 2020



View Online



Export Citation



CrossMark

Biswapriyo Das  and Santanu Mahapatra <sup>a)</sup> 

## AFFILIATIONS

Nano-Scale Device Research Laboratory, Department of Electronic Systems Engineering, Indian Institute of Science (IISc) Bangalore, Bangalore 560012, India

<sup>a)</sup> Author to whom correspondence should be addressed: [santanu@iisc.ac.in](mailto:santanu@iisc.ac.in)

## ABSTRACT

First-principles-based device models are in demand in the semiconductor industry to assess the impact of new materials at very early phases of the technology development. Existing models for the 2D metal–oxide–semiconductor field-effect transistor work under quasi-static limit and can only be used for designing circuits operating under half of the transistor’s intrinsic cut-off frequency. Here, we develop a compact device model for phosphorene-based transistor that takes into account its band structure anisotropy as well as the carrier inertia, which is crucial for high-frequency operation. In a multi-scale approach, density functional theory based calculation is first carried out to obtain the material specific parameters, which are then used to develop a continuity equation based non-quasi-static model to gain insight into the high-frequency behaviors. We find that channel orientation has a strong impact on both the low and high frequency conductances; however, it affects only the high-frequency component of capacitances. The model is then implemented in an industry-standard circuit simulator using relaxation-time-approximation technique and simulations are conducted to demonstrate its applicability for near cut-off frequency circuit operation. The proposed modeling methodology, which connects material to circuit, thus helps us to expand the design space, where technology downscaling could be very challenging and expensive.

Published under license by AIP Publishing. <https://doi.org/10.1063/5.0030633>

## I. INTRODUCTION

After the first demonstration<sup>1</sup> a decade ago, two-dimensional (2D) semiconductor-based field-effect transistors are now being considered as viable options for CMOS (complementary metal–oxide–semiconductor) technology extension.<sup>2</sup> High quality growth technologies<sup>3</sup> for such materials are also in progress for practical realization of integrated circuits. While MoS<sub>2</sub> attracted the primary attention, now other materials like transitional metal chalcogenides,<sup>4–11</sup> phosphorene,<sup>12–15</sup> tellurene,<sup>16,17</sup> etc., are also being explored for transistor fabrication. Hundreds of such atomically thin materials are available with commercial vendors,<sup>18,19</sup> and thousands of them are predicted alongside by computational exfoliation techniques.<sup>20–22</sup> Since the process integration of any new material is a time-consuming and capital-intensive affair in the semiconductor industry, it is very important to assess their impact on integrated circuit performance at a very early stage of the technology development. First-principles-based multiscale models,<sup>23,24</sup> which enable systematic performance evaluation of any new material at device and circuit levels even in the absence of any

experimental data, are thus in demand. Although the initial applications of 2D MOSFETs (metal–oxide–semiconductor field-effect transistors) were targeted toward digital circuits,<sup>25,26</sup> now they are also being explored for analog/RF (radio frequency) circuit applications.<sup>12–14,27,28</sup> In this aspect, existing device models<sup>29–33</sup> are built upon quasi-static (QS) approximations, which neglect the inertia of the charge carriers (i.e., the transit time from the source to the drain). As a result, they become applicable for circuits, operating only under half of the intrinsic cut-off frequency  $f_T$  (frequency, at which, the magnitude of short-circuit current gain of the transistor falls to unity) of the transistor. Requirement of higher frequency circuit design thus forces the designer to adopt smaller technology nodes, which could be very challenging<sup>15,34–36</sup> and thus expensive for 2D material-based technologies. At the same time, availability of high mobility 2D materials, which will lead to high  $f_T$  transistors, is limited. A recent first-principles-based study<sup>37</sup> connotes a similar argument, inferring that relatively high “density of scatterings” is what causes the universally low mobilities in 2D semiconductors with parabolic electron dispersions. Even, low

effective-mass materials like phosphorene, initially predicted to have high carrier mobilities,<sup>38,39</sup> was later found to feature disappointingly low values.<sup>40,41</sup> It is, therefore, important to develop models, which will enable the designer to utilize the entire frequency range (at least up to  $f_T$ ) of the transistor for the circuit design.

In this work, we develop a device model that can predict the channel-orientation-dependent high-frequency performance of 2D MOSFETs and circuits solely from their crystallographic information. Under a multiscale modeling framework, we start with the density functional theory (DFT) calculations of the channel material in order to calibrate a two-band Hamiltonian, which is thereafter employed to formulate a continuity equation (CE) based non-quasi-static (NQS) model under the drift-diffusion (DD) formalism.<sup>42,43</sup> The simple mathematical description exclusively comprehends the subtleties of the Fermi–Dirac (FD) statistics and associated bias-dependent diffusivity,<sup>23</sup> which are overlooked in most of the existing models.<sup>44–46</sup> The proposed model is thereafter used to probe the high frequency behavior of large and small-signal parameters of the transistor and then, using the relaxation-time-approximation (RTA) technique,<sup>47,48</sup> it is implemented in an industry-standard circuit simulator. Dynamic simulations of inverter and amplifier circuits are conducted to exemplify the necessity of NQS models over the QS approximations for the near- $f_T$  circuit design. Although the model is demonstrated for a phosphorene-based transistor, it can, however, be generalized for any 2D material.

## II. RESULTS AND DISCUSSION

### A. Energy dispersion and anisotropic properties of phosphorene

Ever since the first experimental realization of few-layer black phosphorus RF transistors with  $f_T = 12$  GHz by Wang *et al.*<sup>13</sup> phosphorene has been suggested as a potent candidate for RF applications.<sup>12,14</sup> Phosphorus is a pnictogen and phosphorene is the 2D counterpart of its most stable allotrope—the black phosphorus. Unlike the atomic flatness and semi-metallic character of pristine graphene, monolayer phosphorene has rather a puckered honeycomb crystal structure with four  $sp^3$ -hybridized phosphorus atoms in a unit cell and it features a bandgap of 0.9–1.6 eV (subject to different first-principles calculations<sup>39,49–51</sup>). Shown in Fig. 1(a) is a schematic representation (top view) of monolayer phosphorene supercell with armchair and zigzag directions indicated. The variable transport direction in our model is at an angle  $\theta$  ( $0^\circ \leq \theta \leq 90^\circ$ ) with respect to the armchair direction. Figure 1(b) depicts the rectangular first Brillouin zone of phosphorene along with four high-symmetry points, viz.,  $\Gamma$ , X, Y, and L with  $\Gamma$  being the zone centre where the direct bandgap appears. Perhaps, the most fascinating characteristic of phosphorene is the anisotropic carrier transport, originating from the high degree of anisotropy in energy band structures along different crystallographic directions.<sup>39,41,49,51–54</sup> Such an anisotropic property may be exploited to design high-performance integrated circuits in a smaller foot-print on the wafer.<sup>55</sup> As an obvious result of such anisotropic energy dispersion, the carrier effective masses in phosphorene become largely different along armchair (light mass) and zigzag (heavy mass) directions. In

fact, the severe flatness of hole dispersion along the zigzag ( $\Gamma - Y$ ) direction causes large discrepancy in momentum effective-mass values reported earlier.<sup>39,49,56</sup> Nevertheless, the band structure anisotropy is clearly evident from Figs. 1(c) and 1(d) that, respectively, illustrate the elliptic iso-energy contours of conduction and valence bands near the  $\Gamma$  point as obtained from the DFT calculations (see Methods). Also to be noted from Fig. 1(d) is that the anisotropy is more pronounced in the valence band, making directional hole effective masses even more contrasting as compared to the electron effective masses.

Near the  $\Gamma$  point, the top-most valence and bottom-most conduction bands of phosphorene are predominantly contributed by  $p$  orbitals and under the  $k \cdot p$  approximation, the low-energy Hamiltonian ( $H$ ) near the zone centre can be written as<sup>52</sup>

$$H = \begin{pmatrix} E_C + \eta_C k_x^2 + v_C k_y^2 & \gamma k_x + \alpha k_x^2 + \beta k_y^2 \\ \gamma^* k_x + \alpha k_x^2 + \beta k_y^2 & E_V + \eta_V k_x^2 + v_V k_y^2 \end{pmatrix}, \quad (1)$$

where  $E_C$  and  $E_V$ , respectively, denote the energies of conduction band minima and valence band maxima at the  $\Gamma$  point;  $k_x, k_y$  are the wave-vectors;  $\gamma$  is the coupling constant between conduction and valence bands indicating first order correction;  $\alpha, \beta$  define leading order correction terms for interband coupling; and  $\eta_{C(V)}, v_{C(V)}$  represent the respective mass-terms along  $k_x$  and  $k_y$  directions of conduction (subscript C) and valence (subscript V) bands. However, close to the  $\Gamma$  point, interband couplings can be safely ignored ( $\alpha = \beta = \gamma = 0$ ) without losing the essential physics, and the energy dispersions of phosphorene can, therefore, be written as

$$E_{\pm}(k_x, k_y) = \pm \left[ \Delta_{C(V)} + \frac{\hbar^2 k_x^2}{2m_{e(h)x}} + \frac{\hbar^2 k_y^2}{2m_{e(h)y}} \right]. \quad (2)$$

Here,  $E_+$  and  $E_-$ , respectively, stand for electron and hole dispersions,  $\Delta_{C(V)} (= \pm E_{C(V)})$  represents respective energy offsets of conduction (subscript C) and valence (subscript V) band extrema from the Fermi level (set to 0 eV),  $\hbar$  is the modified Planck's constant, and  $m_{e(h)x} (= \pm \hbar^2/2\eta_{C(V)})$ ,  $m_{e(h)y} (= \pm \hbar^2/2v_{C(V)})$ , respectively, denote the electron (subscript e) and hole (subscript h) effective masses along armchair (subscript x) and zigzag (subscript y) directions. Comparisons between the iso-energy contours obtained from Eq. (2) and *ab initio* calculations are provided in Fig. S1 (see the supplementary material). Equation (2) is generic to any 2D material having elliptic iso-energy contours. The numeric values of  $m_{ex}, m_{hx}, m_{ey}$ , and  $m_{hy}$  as obtained from DFT calculations (see Methods) are, respectively,  $0.137m_0, 0.131m_0, 1.26m_0$ , and  $15.477m_0$  with  $m_0$  being the rest mass of electron, whereas both  $\Delta_C$  and  $\Delta_V$  were measured to be 0.467 eV, making a bandgap ( $\Delta_C + \Delta_V$ ) of 0.934 eV. These numbers are in good agreement with earlier report.<sup>41</sup>

### B. Quasi-static model

Here, we develop the core model for the phosphorene-based MOSFET with a conventional gate stack. Non-ideal effects arising from impurities, defects, finite contact resistance, and substrate imperfections are not taken into account since they are process

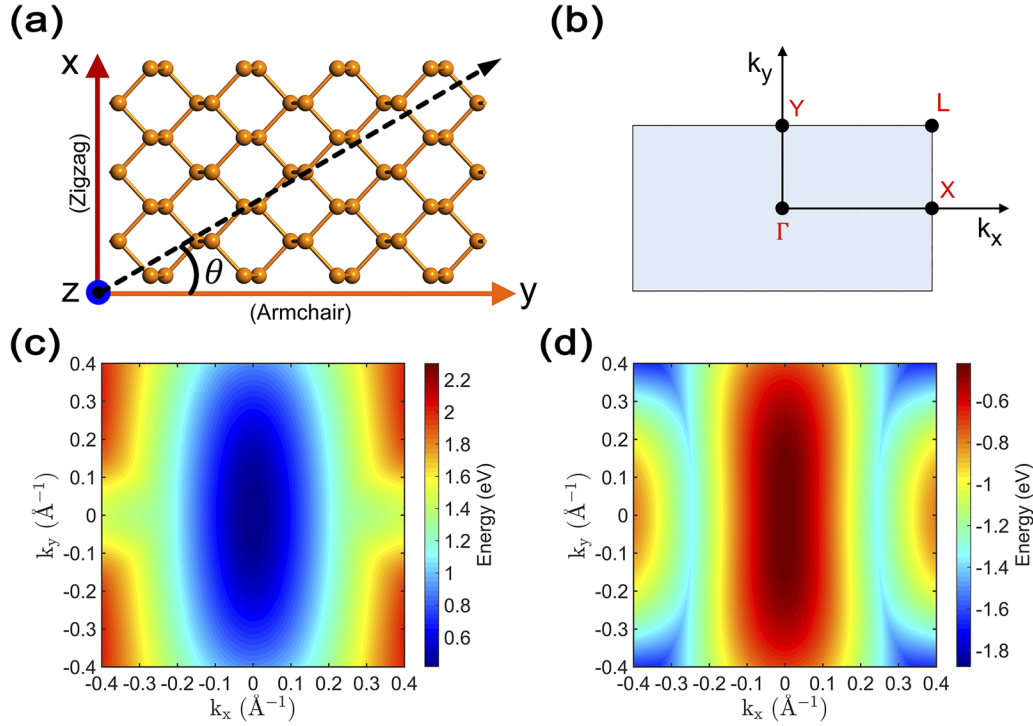


**FIG. 1.** (a) A phosphorene supercell indicating armchair and zigzag directions. The transport direction is at an angle  $\theta$  with respect to the armchair direction. (b) The rectangular first Brillouin zone of phosphorene with the high-symmetry points indicated. The fundamental electronic bandgap appears at the zone centre, i.e., at the  $\Gamma$  point. (c) and (d), respectively, depict the elliptic constant energy contours of conduction and valence bands of phosphorene. The elliptic nature indicates the anisotropy in electron and hole effective masses along  $k_x$  and  $k_y$  directions. (d) indicates that the band structure anisotropy is more pronounced in hole dispersion.

technology dependent and difficult to predict from first-principles. However, they can later be added atop the core model using suitable correction techniques.<sup>57–59</sup> Also, the phosphorene channel is assumed to be pristine, although the effects of doping can easily be addressed by emulating electrostatic doping in first-principles calculations.<sup>23</sup> The effective oxide thickness of the transistor is taken as 0.5 nm, whereas both the length ( $L$ ) and width ( $W$ ) of the channel are to be considered as  $1\ \mu\text{m}$  unless otherwise mentioned.

We start developing the compact model by deriving the expression of electron density of states (DOS) in phosphorene. In general, the expression of 2D DOS ( $g_{2D}$ ) for a single energy band is given by

$$g_{2D}(E') = \frac{g_s g_v}{(2\pi)^2} \int_{-\infty}^{\infty} \int_0^{2\pi} |J| \times \delta(E - E') d\phi dE, \quad (3)$$

where  $E'$  is the electron energy,  $g_s$  and  $g_v$ , respectively, denote spin ( $=2$  for electron) and valley ( $=1$  for  $\Gamma$  valley in phosphorene) degeneracies, and  $J$  represents the Jacobian of transformation from Cartesian ( $k_x, k_y$ ) to polar ( $E, \phi$ ) coordinates. Thereby using the Herring–Vogt<sup>60</sup> transformation, i.e.,  $k_x = \sqrt{m_{ex}} k'_x$ ,  $k_y = \sqrt{m_{ey}} k'_y$  and putting  $E_+ - \Delta_C = E'$  and  $J = \sqrt{m_{ex} m_{ey}} / \hbar^2$ , we get the

expression of electron DOS (per unit area) in phosphorene as  $g_{2D} = \frac{g_s g_v}{2\pi \hbar^2} \sqrt{m_{ex} m_{ey}}$ . The FD statistics can now be employed to formulate the intrinsic carrier (electron) concentration ( $n_0$ ) as  $n_0 = \int_{E_C}^{\infty} g_{2D} \frac{1}{1 + e^{(E - E_F)/k_B T}} dE$  and the resulting expression of  $n_0$  is noted below

$$n_0 = g_{2D} k_B T \ln \left[ 1 + \exp \left( -\frac{\Delta_C}{k_B T} \right) \right]. \quad (4)$$

Here,  $k_B$  is the Boltzmann constant,  $T$  ( $=300\ \text{K}$ ) is the operating temperature,  $E_F$  is the Fermi energy, and  $\Delta_C = E_C - E_F$ .

The electrical equivalent circuit of the metal–oxide–semiconductor (MOS) capacitor can be perceived as a series-connected network of two capacitors:  $C_{OX}$  (oxide capacitance per unit area) and  $C_{qP}$  (quantum capacitance of phosphorene per unit area). Now, upon application of the bias voltages  $V_G$  and  $V_D$ , respectively, at gate and drain terminals (with source terminal grounded), the net electron concentration in the channel ( $n_{net}$ ) can be written using Eq. (4) as

$$n_{net} = g_{2D} k_B T \ln \left[ 1 + \exp \left( -\frac{\Delta_C}{k_B T} + \frac{q(\psi_S - V_{CB})}{k_B T} \right) \right], \quad (5)$$

where  $q$  is electronic charge,  $\psi_S$  is the potential drop across  $C_{qP}$  and  $V_{CB}$  is the channel potential or imref. Thus, the inversion charge density in the channel  $Q'_I$  can be written as  $Q'_I = -qn_{net}$ . On the other hand, owing to the atomic-scale thickness of monolayer phosphorene, the charge distribution in the channel region can be approximated as an ideal 2D sheet,<sup>23</sup> which simplifies the solution of Poisson's equation straight ahead. The work function difference between the gate and channel material is taken into account by representing  $V_G$  as  $V_G = V_{G,appl} - V_{FB}$ , where  $V_{G,appl}$  is the actual applied voltage at gate terminal and  $V_{FB}$  is the flatband voltage. Now, the potential ( $V_G = \psi_{OX} + \psi_S$ ) and charge ( $Q'_G + Q'_I = 0$ ) balance equations of the device lead to the following surface potential equation:

$$(V_G - \psi_S) - \frac{qg_{2D}k_B T}{C_{OX}} \ln \left\{ 1 + \exp \left[ -\frac{\Delta_C}{k_B T} + \frac{q(\psi_S - V_{CB})}{k_B T} \right] \right\} = 0, \quad (6)$$

where  $\psi_{OX} = Q'_G/C_{OX}$  is the potential drop against oxide layer and  $Q'_G$  symbolizes the gate charge density. An approximate yet accurate closed-form solution of Eq. (6) is discussed in the [supplementary material](#). Having obtained a solution for  $\psi_S$ ,  $C_{qP}$  can now be evaluated using the following expression:

$$C_{qP} = q^2 g_{2D} \times \left[ 1 + \exp \left( \frac{\Delta_C}{k_B T} - \frac{q(\psi_S - V_{CB})}{k_B T} \right) \right]^{-1}. \quad (7)$$

To be noted that, if the exponent of Eq. (7) is negligibly small ( $\ll 0$ ), then  $C_{qP}$  achieves the quantum capacitance limit of  $q^2 g_{2D}$ .

Now, we adopt the semiclassical DD formalism<sup>42,43</sup> to model the DC drain current ( $I_{DC}$ ) and terminal charges  $Q_T$  ( $T = G, D, S$ , respectively, denoting gate, drain, and source terminals). Under DD formalism, the expression of  $I_{DC}$  reads

$$I_{DC} = \frac{W}{L} \left[ \mu_e \int_{\psi_{S0}}^{\psi_{SL}} (-Q'_I) d\psi_S + D_e \int_{Q'_{I0}}^{Q'_{IL}} dQ'_I \right], \quad (8)$$

where  $\mu_e$  and  $D_e$ , respectively, denote the low-field mobility and bias-dependent diffusivity of electron in phosphorene and  $\psi_{S0}$  ( $\psi_{SL}$ ),  $Q'_{I0}$  ( $Q'_{IL}$ ) symbolize the respective values of  $\psi_S$  and  $Q'_I$  at source (drain) end of the channel. Since we are interested in closed-form expressions of the drain current and terminal charges to facilitate implementation in a circuit simulator, the transport equation is, therefore, solved independently from the electrostatic solution [Eq. (6)], which is a common practice in compact modeling. Explicit involvement of FD statistics in our model necessitates the incorporation of bias-dependent character of  $D_e$ ,<sup>23</sup> which, in turn, increases the complexity of model equations. Earlier 2D transistor models completely ignored this subtlety.<sup>29,31,33,44</sup> The definition of bias-dependent  $D_e$ , i.e.,  $D_e = \mu_e Q'_I (d\psi_S/dQ'_I)|_{V_{DS}=0}$  ensures zero drain current at zero drain bias. We derive the expression of bias-

dependent diffusivity as

$$D_e = \mu_e \frac{k_B T}{q} \ln \left\{ 1 + \exp \left( -\frac{\Delta_C}{k_B T} + \frac{q\psi_S}{k_B T} \right) \right\} \times \left[ 1 + \exp \left( \frac{\Delta_C}{k_B T} - \frac{q\psi_S}{k_B T} \right) \right]. \quad (9)$$

In terms of carrier mobilities in phosphorene, the theoretically predicted numbers<sup>39,41,49,50,56</sup> are, however, not only in sheer disagreement with the experimental results,<sup>40,53,61</sup> but also the theoretical predictions themselves contradict with each other substantially. Synopsizing several key-reports in this context, Gaddemane *et al.*<sup>41</sup> identified possible reasons for such counterstatements and thereafter in the spirit of accurate full-band Monte Carlo simulations, they emphasized the cruciality of considering angle-dependent deformation potentials in mobility calculations over its constant counterpart, considered hitherto. Their findings suggest that, a free-standing monolayer phosphorene features rather inferior mobility profiles; for example, electron mobilities in phosphorene are  $20 \text{ cm}^2/V\text{s}$  in the armchair direction and  $10 \text{ cm}^2/V\text{s}$  in the zigzag direction, whereas hole mobilities are even smaller. Nevertheless, calibrating the anisotropic electron mobility profile reported in Ref. 41, we manifest the angle-dependence of  $\mu_e$  as

$$\mu_e = \left( \frac{\mu_{eAC} + \mu_{eZZ}}{2} \right) + \left( \frac{\mu_{eAC} - \mu_{eZZ}}{2} \right) \cos(2\theta), \quad (10)$$

where  $\mu_{eAC}$  and  $\mu_{eZZ}$  denote the values of  $\mu_e$ , respectively, in armchair ( $\theta = 0^\circ$ ) and zigzag ( $\theta = 90^\circ$ ) directions. Furthermore, since  $D_e$  explicitly depends on  $\mu_e$ , it becomes a function of  $\theta$  as well. The variation of  $D_e$  with respect to  $\theta$  is depicted in Fig. 2(a) with  $V_G$  as a parameter. It clarifies that at  $V_G = 0 \text{ V}$ , the well-known expression of  $D_e = \mu_e \frac{k_B T}{q}$  holds; however, the bias-dependent character of  $D_e$  becomes evident as  $V_G$  increases. Also, it shows that variation of  $D_e$  as a function of  $\theta$  becomes more pronounced as  $V_G$  increases monotonically. For example, at  $V_G = 1 \text{ V}$ ,  $D_e$  is almost thrice greater than the bias-independent value for  $\theta = 0^\circ$ , although lower mobility along the zigzag direction restricts  $D_e$  to only  $11 \times 10^{-5} \text{ m}^2/\text{s}$ .

In the course of deriving a closed-form expression of  $I_{DC}$ , we first deduce  $Q'_I(V_G, V_{CB}) = -C_{OX}[V_G - \psi_S(V_G, V_{CB})]$  from the potential and charge balance conditions. Since, under our charge-sheet approximation,  $\psi_S$  is invariant along the direction, perpendicular to the transport direction  $x$ , we can, therefore, write  $d\psi_S = (1/C_{OX})dQ'_I$ . Thereby using Eq. (8),  $I_{DC}$  can be formulated as

$$I_{DC} = \frac{W}{L} \mu_e \left\{ -\frac{1}{2C_{OX}} (Q'^2_{IL} - Q'^2_{I0}) + \tilde{D}_e (Q'_{IL} - Q'_{I0}) \right\}, \quad (11)$$

where  $\tilde{D}_e = D_e/\mu_e$ . However, it is noteworthy that either in presence of the semiconductor body charge,<sup>43</sup> gate depletion effect,<sup>43</sup> finite gate quantum capacitance,<sup>23</sup> or even for asymmetric multi-gate architectures,<sup>62</sup>  $Q'_I$  may not hold a linear relationship with  $\psi_S$  implying  $d\psi_S \neq (1/C_{OX})dQ'_I$ . Such a non-linear profile invokes the implementation of suitable linearization techniques.<sup>23,43</sup>

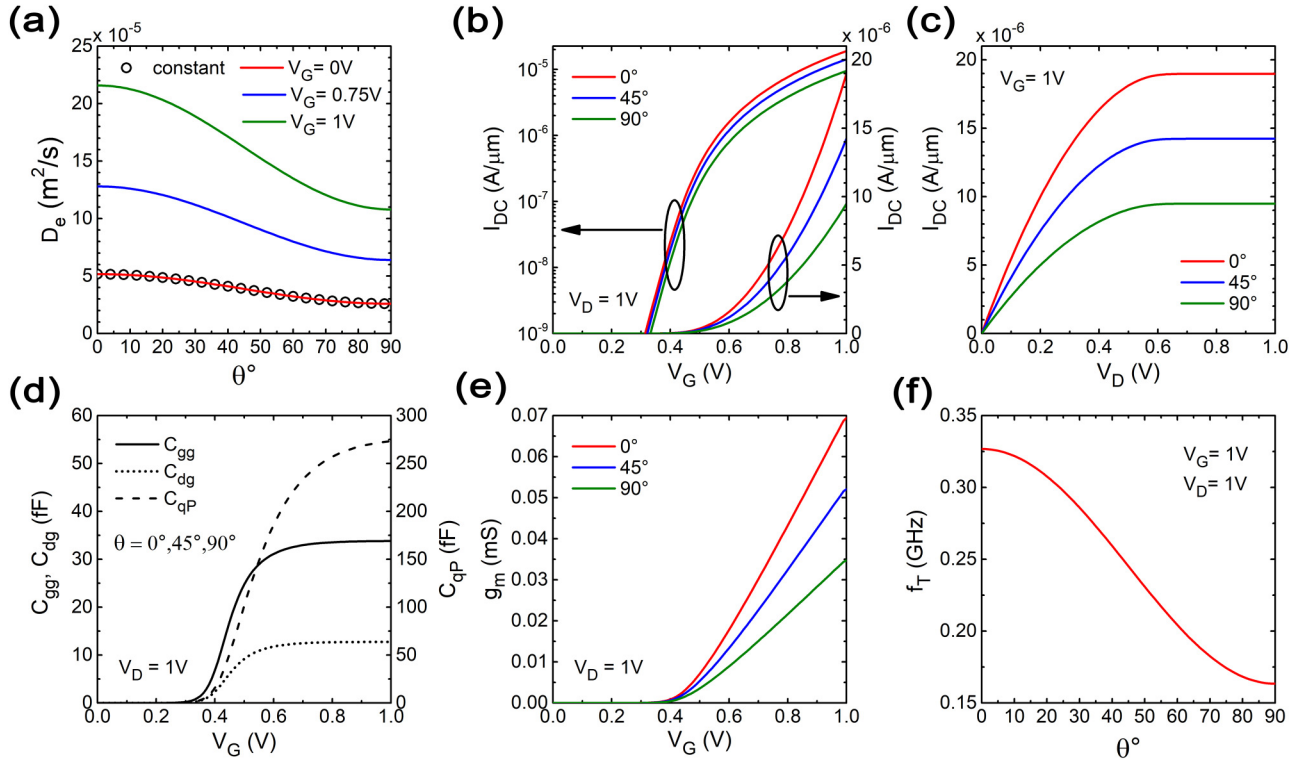


**FIG. 2.** (a) represents the bias-dependent electron diffusivity profile of phosphorene with respect to the variable transport direction  $\theta$ .  $\theta = 0^\circ$  and  $\theta = 90^\circ$ , respectively, indicate the armchair and zigzag directions. The constant diffusivity, as can be obtained from the Einstein's formula ( $D_e = \mu_e k_B T/q$ ), coincides with the bias-dependent diffusivity profile for  $V_G = 0$  V and as depicted in (a), the bias-dependent diffusivity increases with increasing gate voltage. (b) and (c), respectively, illustrate the  $\theta$ -dependent DC transfer and drain characteristics of the phosphorene transistor for the  $1 \mu\text{m}$  channel length. Maximum mobility along  $\theta = 0^\circ$  results into a maximum saturation current of  $\sim 19 \mu\text{A}/\mu\text{m}$ . (d) represents the transcapacitance ( $C_{gg}$  and  $C_{dg}$ ) and quantum capacitance ( $C_{qp}$ ) profiles of phosphorene as a function of gate bias. The transcapacitance profiles were found to be  $\theta$ -invariant for DC and low frequency operations. (e) showcases different  $g_m - V_G$  profiles for  $\theta = 0^\circ, 45^\circ$ , and  $90^\circ$ . (f) demonstrates the variation of intrinsic cut-off frequency  $f_T$  with respect to  $\theta$  at transistor saturation. The variation of  $f_T$  resembles the mobility profile of phosphorene.

Figures 2(b) and 2(c), respectively, illustrate the transfer and drain characteristics of the transistor, where directional nonuniformity of  $\mu_e$  and  $D_e$  results into variations in current-voltage profiles for different  $\theta$ . Maximum mobility along the armchair direction yields a maximum saturation current of  $\sim 19 \mu\text{A}/\mu\text{m}$  for  $\theta = 0^\circ$  at  $V_G = V_D = 1$  V, whereas the same is  $\sim 9.5 \mu\text{A}/\mu\text{m}$  for  $\theta = 90^\circ$ . The subthreshold swing of the device, calculated to be  $\sim 72$  mV/dec, however, remains almost unaltered as  $\theta$  is varied. Apart from this, the threshold voltage ( $\sim 0.5$  V) of the transistor was also found to be  $\theta$ -invariant since it depends only on the DOS of the channel material.

Now, by the principle of current continuity, the above form of drain current [Eq. (11)] can be generalized for any point  $x$  ( $0 \leq x \leq L$  with  $x = 0$  and  $x = L$ , indicating source and drain ends, respectively) in the channel as  $I_{DC} = \frac{W}{x} \mu_e \{F(Q'_{lx}) - F(Q'_{l0})\}$ , where  $F(Q'_{lx})$  is given by  $F(Q'_{lx}) = -\frac{Q'_{lx}}{2C_{ox}} + \bar{D}_e Q'_{lx}$  with  $Q'_{lx}$  being the value of  $Q'_l$  at point  $x$ . Therefore, the position along the channel, i.e.,  $x$  becomes a quadratic function of the inversion charge density, expressed as:  $x(Q'_{lx}) = L \frac{F(Q'_{lx}) - F(Q'_{l0})}{F(Q'_{ll}) - F(Q'_{l0})}$ . This analytic

relationship is very useful to develop terminal charge models for both QS and NQS cases as will be demonstrated later. Now, according to Ward-Dutton<sup>63</sup> charge partitioning scheme, the definitions of terminal charges read:  $Q_G = -W \int_0^L Q'_{lx} dx$ ,  $Q_D = W \int_0^{\frac{x}{L}} Q'_{lx} dx$ , and  $Q_S = W \int_0^L (1 - \frac{x}{L}) Q'_{lx} dx$ . Finally, using these terminal charge profiles, we can express the respective terminal currents under time ( $t$ )-varying external bias as  $I_G(t) = \frac{d}{dt}(Q_G(t))$ ,  $I_D(t) = I_{DC}(t) + \frac{d}{dt}(Q_D(t))$ , and  $I_S(t) = -I_{DC}(t) + \frac{d}{dt}(Q_S(t))$ . Here, we have considered the directions of all terminal currents to be entering into the device.

When the terminal voltages change with time,  $Q'_{lx}$  becomes an explicit function of  $x$  and  $t$ . However, under QS approximation, i.e., when the terminal voltages vary much slower than the transit time of the carriers ( $\tau \approx L^2/\mu_e V_D$ ) from source to drain, the explicit dependence of  $Q'_{lx}$  on  $t$  can be safely neglected. Under such a condition, using the aforementioned  $x$  vs  $Q'_{lx}$  quadratic relationship, the terminal

charges can be formulated as

$$Q_{G,QS} = -WL \times \frac{2(Q'_{IL}{}^3 - Q'_{I0}{}^3) - 3\tilde{D}_e C_{OX}(Q'_{IL}{}^2 - Q'_{I0}{}^2)}{3(Q'_{IL}{}^2 - Q'_{I0}{}^2) - 6\tilde{D}_e C_{OX}(Q'_{IL} - Q'_{I0})}, \quad (12a)$$

$$Q_{D,QS} = WL \times [30(Q'_{IL}{}^2 - Q'_{I0}{}^2)^2 + 120\tilde{D}_e^2 C_{OX}^2(Q'_{IL} - Q'_{I0})^2 - 120\tilde{D}_e C_{OX}(Q'_{IL} - Q'_{I0})(Q'_{IL}{}^2 - Q'_{I0}{}^2)]^{-1} \times [12(Q'_{IL}{}^5 - Q'_{I0}{}^5) - 20Q'_{I0}{}^2(Q'_{IL}{}^3 - Q'_{I0}{}^3) - 5\tilde{D}_e C_{OX} \times \{9(Q'_{IL}{}^4 - Q'_{I0}{}^4) - 8(\tilde{D}_e C_{OX} + Q'_{I0})(Q'_{IL}{}^3 - Q'_{I0}{}^3) + 6Q'_{I0}(2\tilde{D}_e C_{OX} - Q'_{I0})(Q'_{IL}{}^2 - Q'_{I0}{}^2)\}], \quad (12b)$$

$$Q_{S,QS} = -(Q_G + Q_D). \quad (12c)$$

Figure 2(d) exhibits the plots of  $C_{gg}$  (total capacitance as seen from the gate terminal),  $C_{qp}$ , and the transcapacitance  $C_{dg}$  as a function of  $V_G$  ( $V_D = 1$  V), whereas the transconductance ( $g_m$ ) profile with respect to  $V_G$  ( $V_D = 1$  V), calculated as  $g_m = \partial I_{DC} / \partial V_G$ , is showcased in Fig. 2(e). The terminal capacitances ( $C_{XY}$ ) were calculated as  $C_{XY} = \partial Q_X / \partial V_Y$ , where  $Q_X$  and  $V_Y$  are, respectively, the terminal charge and voltage at X and Y terminals.  $C_{gg}$ , however, can also be formulated as  $C_{gg} = (1/C_{OX} + 1/C_{qp})^{-1}$ , which for  $V_D = 1$  V is mostly dictated by  $C_{OX}$  when  $V_G$  is less than the threshold voltage.  $C_{qp}$ , on the other hand, was found to operate always within the quantum capacitance limit as mentioned before. The  $g_m - V_G$  profiles of Fig. 2(e) vary with  $\theta$  because  $g_m$  inherently depends on  $I_{DC}$ , which, in turn, depends on the mobility. The maximum value of  $g_m$  for  $\theta = 0^\circ$  was found to be 0.07 mS. The profiles of drain conductance ( $g_D$ ) and transcapacitance  $C_{gd}$  are provided in Fig. S2 (see the supplementary material). However, it is noteworthy that, although the terminal capacitance profiles hereby seem to be  $\theta$ -independent as because they solely depend on  $g_{2D}$  and not explicitly on  $\mu_e$ , later it will be revealed that they actually become functions of  $\theta$  at high frequencies ( $> 0.1$  GHz).

In saturation condition ( $V_G = V_D = 1$  V), the intrinsic cut-off frequency  $f_T$  can be calculated from the QS model using  $f_T = \frac{g_m}{2\pi C_{gs}}$  and the resulting  $f_T$  vs  $\theta$  profile is portrayed in Fig. 2(f). Needless to say, the angular dependence of  $f_T$  originates from the aforesaid angle-dependent mobility profile. The maximum value of  $f_T$  was obtained to be 0.33 GHz for  $\theta = 0^\circ$ , whereas it falls to 0.24 GHz and 0.16 GHz, respectively, for  $\theta = 45^\circ$  and  $90^\circ$ .

### C. Non-quasi-static model

The essence of NQS treatment gains attention particularly at high frequencies when the transistor behavior cannot be treated as successive steady-state situations anymore. An NQS model necessarily takes into account the inertia of charge carriers, thus acknowledging the finite carrier transit time from source to drain. Thereby, all the relevant quantities become explicitly time-dependent.

There are two different widely-accepted approaches to model NQS effects in conventional transistors. The CE based approach<sup>64–69</sup> is governed by the principle of current continuity in transistor channel and is purely physics-based. It does not involve additional model parameter extraction other than the ones used in its QS counterpart. However, this method is mathematically complex and thus challenging for implementation in a circuit simulator. On the other hand, the phenomenological RTA<sup>47,48</sup> based methodology accounts for the transit time delay by defining a carrier relaxation time using additional semiempirical model parameters, which need to be calibrated from the high-frequency response of the transistor. This technique is easy to implement in circuit simulators since the mathematical expressions are much simpler. Here, the CE based approach will be first exercised to develop the NQS model atop the aforesaid QS counterpart, duly addressing the anisotropic properties of phosphorene. However, the perception of bias-dependent diffusivity significantly increases the complexity of model equations and eventually spoils its implementation in circuit simulators. This issue was thereafter addressed using the RTA based approach.

For the NQS operation, both the channel charge and current become explicit functions of time  $t$  and position  $x$  in the channel and could be expressed as

$$Q'_i(x, t) = -C_{OX}[V_G(t) - \psi_S(x, t)], \quad (13)$$

$$I(x, t) = W \left[ -\mu_e Q'_i(x, t) \frac{\partial \psi_S(x, t)}{\partial x} + D_e(t) \frac{\partial Q'_i(x, t)}{\partial x} \right]. \quad (14)$$

On the other hand, the current continuity equation (neglecting the generation-recombination process) is given by

$$\frac{\partial I(x, t)}{\partial x} = W \frac{\partial Q'_i(x, t)}{\partial t}. \quad (15)$$

Now using  $\frac{\partial \psi_S}{\partial x} = \frac{1}{C_{OX}} \frac{\partial Q'_i}{\partial x}$  from Eq. (13) in the first derivative (with respect to  $x$ ) of Eq. (14) and then combining it with Eq. (15), we get

$$\frac{1}{\rho} \frac{\partial Q'_i(x, t)}{\partial t} = \left( \frac{D_e(t)}{\rho} - Q'_i(x, t) \right) \frac{\partial^2 Q'_i(x, t)}{\partial x^2} - \left( \frac{\partial Q'_i(x, t)}{\partial x} \right)^2, \quad (16)$$

where  $\rho = \mu_e / C_{OX}$ . Thereafter, changing the variable  $Q'_i(x, t)$  to  $Q(x, t)$  using  $\frac{D_e(t)}{\rho} - Q'_i(x, t) = Q(x, t)$ , we deduce the final form of the partial differential equation (PDE) as drafted in Eq. (17),

$$\frac{1}{\rho} \frac{\partial Q(x, t)}{\partial t} = \frac{\partial}{\partial x} \left( Q(x, t) \frac{\partial Q(x, t)}{\partial x} \right) + \frac{1}{\rho^2} \frac{\partial D_e(t)}{\partial t}. \quad (17)$$

The second term in R.H.S. of Eq. (17), containing time-derivative of  $D_e$ , adds to the mathematical complexity of the problem because having the knowledge of  $\partial D_e(t) / \partial t$  requires the numeric values of  $D_e$  at different time-stamps in advance. This problem was tackled by writing  $\partial D_e(t) / \partial t$  as  $\frac{\partial D_e}{\partial t} = \frac{\partial D_e}{\partial V_G} \times \frac{\partial V_G}{\partial t}$  and

modeling  $\frac{\partial D_e}{\partial V_G}$  as a rational function of  $V_G$  of degree 5 and then calibrating the coefficients of the polynomials (see the [supplementary material](#)). These calibrations are showcased in Fig. S3 (see the [supplementary material](#)) for  $\theta = 0^\circ$ ,  $45^\circ$ , and  $90^\circ$ , and the coefficients can be found in Table S1 (see the [supplementary material](#)). Due to such perplexity, the  $\partial D_e(t)/\partial t$  term may even complicate the plausible semi-analytical treatments of Eq. (17), reported erstwhile for traditional MOSFETs (the weighted residue method,<sup>70</sup> spline collocation method,<sup>62,66,71,72</sup> or variational techniques<sup>67</sup>). We

solve this nonlinear PDE numerically for  $Q$ , using initial ( $Q(x, 0)$ ) and boundary conditions ( $Q(0, t)$  at  $x = 0$  and  $Q(L, t)$  at  $x = L$ ) assuming that,  $Q'_I$  can change instantaneously at source and drain ends (i.e., no NQS effect is present at the channel ends).<sup>62,67</sup> Therefore, the initial and boundary conditions, derived from the QS profile of  $Q(x, t)$  can be used here. This QS charge profile [Eq. (18)] can be extracted from  $x(Q'_I(t)) = L \frac{F(Q'_I(t)) - F(Q'_{I0}(t))}{F(Q'_{IL}(t)) - F(Q'_{I0}(t))}$  by replacing  $Q'_I(x, t)$  with  $Q(x, t)$  as prescribed before and can be expressed as

$$Q(x, t) = \left[ \left( \frac{D_e(t)}{\rho} - Q'_{I0}(t) \right)^2 + \frac{x}{L} (Q'_{IL}(t) - Q'_{I0}(t)) \left\{ (Q'_{IL}(t) + Q'_{I0}(t)) - \frac{2D_e(t)}{\rho} \right\} \right]^{\frac{1}{2}}. \quad (18)$$

The initial and boundary conditions as deduced from Eq. (18) read

$$Q(x, 0) = \left[ \left( \frac{D_e(0)}{\rho} - Q'_{I0}(0) \right)^2 + \frac{x}{L} (Q'_{IL}(0) - Q'_{I0}(0)) \left\{ (Q'_{IL}(0) + Q'_{I0}(0)) - \frac{2D_e(0)}{\rho} \right\} \right]^{\frac{1}{2}}, \quad (19a)$$

$$Q(0, t) = \frac{D_e(t)}{\rho} - Q'_{I0}(t), \quad (19b)$$

$$Q(L, t) = \frac{D_e(t)}{\rho} - Q'_{IL}(t). \quad (19c)$$

Now, followed by the numerical solution of Eq. (17), the NQS channel charge ( $Q'_{I,NQS}$ ) can subsequently be obtained using  $Q'_{I,NQS}(x, t) = \frac{D_e(t)}{\rho} - Q(x, t)$  and thereafter the NQS terminal charges ( $Q_{T,NQS}$ ) can be derived by numerically integrating  $Q'_{I,NQS}$  according to the Ward–Dutton charge partitioning scheme.

#### D. Large signal transient response

For large signal operations,<sup>73</sup> the input signal variation is chosen to be large enough to produce nonlinear behavior. Here, a trapezoidal pulse  $V_G(t)$ , with a rise and fall time of 1 ns is applied at the gate terminal [see Fig. 3(a)] and  $V_D$  is always kept at 1 V to ensure the transistor saturation. Figure 3(a) illustrates total terminal current profiles (both  $I_{T,QS}$  and  $I_{T,NQS}$ ) for large signal operation along different transport directions, viz.,  $\theta = 0^\circ$ ,  $45^\circ$ , and  $90^\circ$ . As can be interpreted at a glance, the envelopes of these current waveforms, emanating from different mobility profiles along those directions, remain invariant of  $\theta$ . Now, before the explanation follows, let us remind that total terminal currents for the source and the drain [i.e.,  $I_{T,QS}(t)$  and  $I_{T,NQS}(t)$  with  $T = S$  or  $D$ ] has two components, viz., the DC current  $I_{DC}(t)$  and the QS or NQS transient component, i.e.,  $\frac{d}{dt}(Q_{T,QS}(t))$  or  $\frac{d}{dt}(Q_{T,NQS}(t))$ , whereas the gate terminal current [i.e.,  $I_{G,QS}(t)$  or  $I_{G,NQS}(t)$ ] has only the transient component  $\frac{d}{dt}(Q_{G,QS}(t))$  or  $\frac{d}{dt}(Q_{G,NQS}(t))$ . Time evolutions of these terminal charge and current components under the applied gate pulse are provided in Fig. S4 (see the [supplementary material](#)). Now, during the turn-on transient, the DC current  $I_{DC}(t)$  increases exponentially with  $V_G$ , once the transistor is in strong inversion.

Since there was no inversion layer present beforehand, NQS effects become significant only after it is formed at the onset of strong inversion. Once the inversion layer is created, electrons get injected into the channel from the source end, but due to high energy barrier, drain terminal fails to do the same. Thus, the drain partition of channel charge ( $Q_{D,NQS}$ ) is rather small but the source charge ( $Q_{S,NQS}$ ) starts to decrease (negative charge build-up) with increasing  $V_G$ . To be noted in this regard that the NQS charge build-up profiles ( $Q_{T,NQS}$ ) have more sluggish signatures than their QS counterparts ( $Q_{T,QS}$ ). However, during this rise time, the electron wavefront injected by the source has not yet reached the drain end due to the channel inertia. This dictates the total drain current  $I_{D,NQS}$  to be equal to zero, whereas the QS approximation (i.e., electrons injected by source, instantaneously reaches the drain end), on the other hand, leads to a non-zero (negative)  $I_{D,QS}$  profile. Nevertheless, since the source end is always injecting electrons into the channel, total source currents (both  $I_{S,QS}$  and  $I_{S,NQS}$ ) are non-zero during this rising ramp. At the end of the rise time, the source as usual continues to inject electrons into the channel (because the energy barrier at the source is low), but those charge-fronts now commence reaching at the drain end. Therefore, the NQS terminal charges ( $Q_{T,NQS}$ ) start reaching the equilibrium gradually, whereas the QS charges ( $Q_{T,QS}$ ) saturate abruptly. This phenomenon effectuates gradual fading of NQS transient current components  $\frac{d}{dt}(Q_{D,NQS}(t))$  and  $\frac{d}{dt}(Q_{S,NQS}(t))$ , abrupt disappearance of QS transient current components  $\frac{d}{dt}(Q_{D,QS}(t))$  and  $\frac{d}{dt}(Q_{S,QS}(t))$ , and gradual (abrupt) saturation of total source current  $I_{S,NQS}$  ( $I_{S,QS}$ ). Finally, at this moment, the charge-front reaches the drain end and the total drain current  $I_{D,NQS}$  starts to flow. After a while, when NQS transient current components vanish, total NQS currents ( $I_{T,NQS}$ ) converge to  $I_{T,QS}$ . The gate current waveforms  $I_{G,NQS}$  and  $I_{G,QS}$ , respectively, follow the similar trends of  $I_{S,NQS}$  and  $I_{S,QS}$  but with an opposite sign, stemming from the way they are defined. However, it is to be noted that, while the waveforms of  $I_{G,QS}$  remain

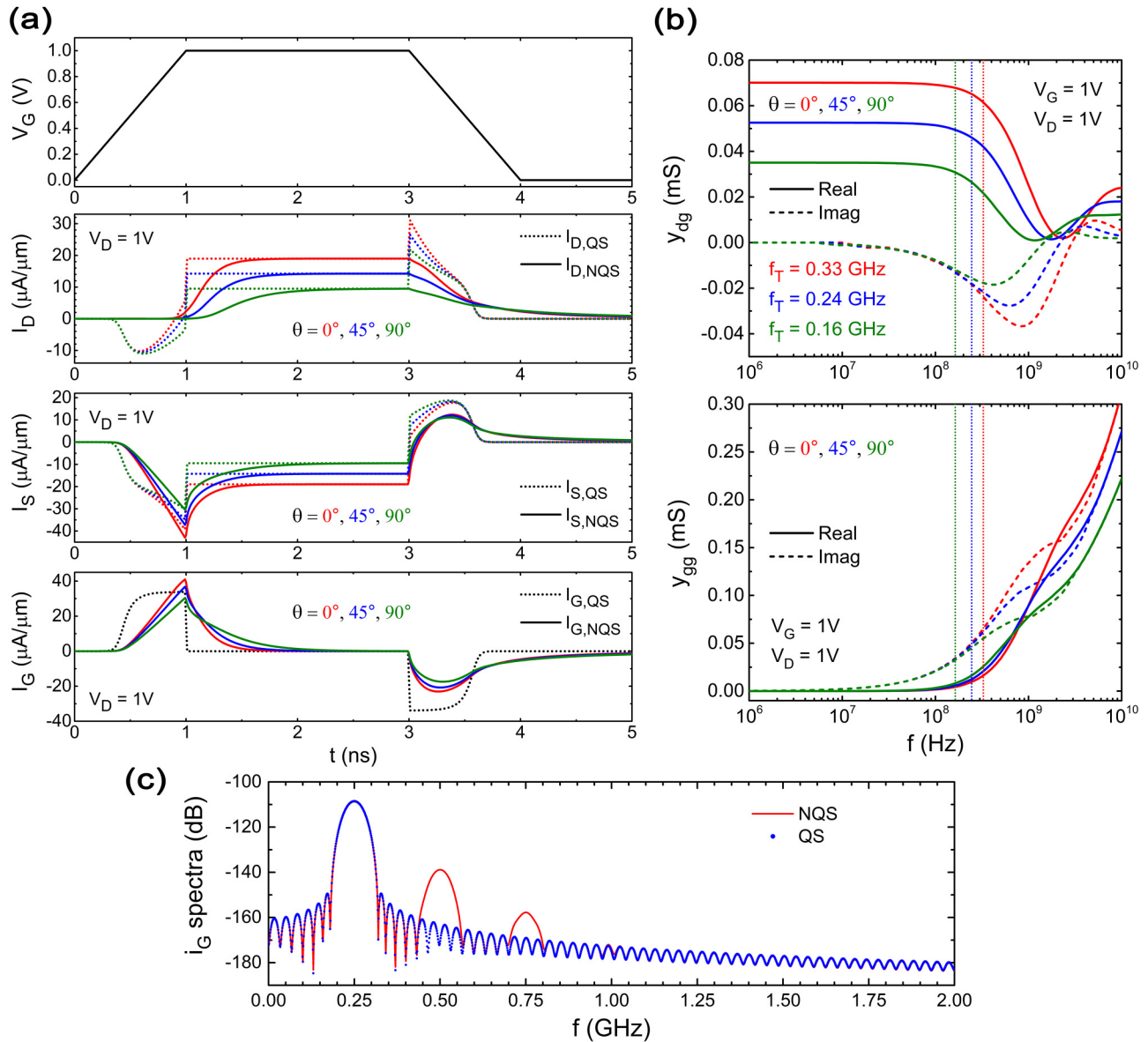


**FIG. 3.** (a) Large signal characteristics of the phosphorene transistor under QS and NQS operations. A trapezoidal pulse  $V_G(t)$  is applied at the gate while keeping  $V_D = 1\text{ V}$ . The terminal current waveforms are shown for  $\theta = 0^\circ, 45^\circ,$  and  $90^\circ$ . For all the current profiles, dotted lines represent the QS operation and solid lines represent the NQS operation. The color scheme (i.e., red for  $0^\circ$ , blue for  $45^\circ$ , and green for  $90^\circ$ ) is the same for all illustrations. As shown in (a), the QS approximations result into unphysical spikes/abrupt changes in current waveforms for fast transients, whereas the NQS model captures the correct gradual transitions. However, for sufficiently slow transients, the NQS model converges to its QS counterpart. (b) illustrates the variations of small-signal parameters  $y_{dg}$  and  $y_{gg}$  as the operating frequency is swept from 1 Hz to 10 GHz. The color scheme is the same as mentioned before. The cut-off frequencies for respective  $\theta$ s are indicated by vertical dotted lines following the same color scheme. In (b), solid and dashed lines, respectively, represent the real and imaginary parts of  $y$ -parameters. (b) illustrates that while the transconductances vary with respect to  $\theta$  both at low and high frequencies, respective transcapacitances differ from each other only at high frequencies. (c) Gate current spectra for harmonic distortion analysis. While the NQS model (solid red line) accurately captures the higher-order harmonics, appearing at terminal current spectra, the QS model (blue dot) underestimates them.

invariant with respect to  $\theta$ , the waveforms of  $I_{G,NQS}$  slightly vary for different transport directions. This variation of  $I_{G,NQS}$  is caused by the orientation-dependent charge inertia, which is captured in  $Q_{G,NQS}$  but not in  $Q_{G,QS}$ .

The scenario is quite different for turn-off transients as because the inversion layer is already present in the channel, which would not vanish until the end of the falling ramp. Thus,  $I_{DC}(t)$  starts to falloff exactly at the onset of the falling ramp. At this

moment, both  $Q_{T,NQS}$  and  $Q_{T,QS}$  at source and drain ends start to increase (reduction of negative charge) to ultimately become zero, which, in turn, causes  $\frac{d}{dt}(Q_{T,NQS}(t))$  to rise gradually and  $\frac{d}{dt}(Q_{T,QS}(t))$  to rise abruptly at first. It results into an unphysical spike in  $I_{D,QS}$  profile and a gradual downfall in the  $I_{D,NQS}$  profile. Then, after a while, when the transistor is about to leave the strong inversion,  $Q_{T,QS}$  diminishes to zero, making  $\frac{d}{dt}(Q_{T,QS}(t))$  as well as the total current  $I_{T,QS}$  vanish immediately. However, this moment in the NQS operation witnesses a gradual decrement of  $\frac{d}{dt}(Q_{T,NQS}(t))$  profiles and, therefore, a longer falling tail appears in  $I_{T,NQS}$  waveforms. The gate current waveforms bear similar characteristics as mentioned before.

In due course of the trapezoidal pulse, the NQS drain charge and drain current lag behind their source counterparts due to the channel inertia and as obvious it is, NQS results came out to be consistently converging to QS profiles for sufficiently slow transients. In a nutshell, the NQS model correctly demonstrates the realistic gradual termination of terminal currents as opposed to the abrupt profiles of the QS model.

### E. Small-signal $y$ -parameter analysis

Small-signal analysis becomes particularly important for designing analog RF circuits and often their high frequency behaviors are characterized by  $y$  (admittance)-parameters, which are complex quantities. By relation,  $y_{XY} = g_{XY} + j\omega C_{XY}$ , where  $X$  and  $Y$  denote device terminals, viz.,  $g$  (gate),  $d$  (drain), or  $s$  (source);  $g_{XY}$  and  $C_{XY}$ , respectively, symbolize the transconductance and transcapacitance parts; and  $\omega = 2\pi f$  with  $f$  being the operating frequency. Although several analytical treatments for small-signal NQS models have been proposed for conventional transistors;<sup>48,64,65,68,69</sup> however, in our case, the bias-dependent nature of  $D_e$  eventually hinders the CE based derivation of closed-form  $y$ -parameter expressions. However, a numerical treatment is always feasible and hereby we perform the same (see the [supplementary material](#)) considering the transistor in the saturation condition.

Figure 3(b) illustrates the low and high frequency characteristics of  $y_{dg}$  and  $y_{gg}$  for different  $\theta$  (see Fig. S5 of the [supplementary material](#) for a comparison between  $y$ -parameter profiles considering bias-dependent  $D_e$  and constant  $D_e$ ). At low frequencies, the channel inertia is negligible and, therefore, the channel charge can respond to small variations in the applied signal quasi-statically. This situation is favorable up to frequency  $f \approx f_T/2$  and that is why, the low frequency tails of  $y$ -parameters necessarily remain invariant with respect to  $f$ . Also, as obvious it is, these low frequency tails ultimately converge to the corresponding conductance or capacitive susceptance values, obtained from the QS condition. For example, at low frequencies, the real part of  $y_{dg}$ , i.e., the transconductance  $g_m$  converges to  $\sim 0.07$  mS for  $\theta = 0^\circ$ , which is equal to its QS value [see Fig. 2(e)] at saturation. However, the imaginary part of  $y_{dg}$ , i.e., the capacitive susceptance  $2\pi f C_{dg}$  becomes vanishingly small at low frequencies because of both small values of  $f$  itself and low transcapacitance ( $C_{dg}$ ) values of about 12 fF [see Fig. 2(d)]. On the other hand, at moderate and high frequencies,  $v_g$  (small signal of amplitude 1 mV, applied at gate terminal) is varying very fast and due to now-non-negligible inertia, the

channel charge does not get enough time to respond to this variation. Therefore, the quantity  $|y_{dg}|$ , which models this response, starts to fall monotonically to ultimately become zero at ultra-high frequencies ( $>100$  GHz). Also, the phase of  $y_{dg}$  starts to drop from zero (meaning no lag at low frequencies) to become negative because the “effect”, i.e., total (DC + small signal) output current from gate terminal  $i_D(t)$  now starts to lag behind the “cause”, i.e., the total gate input voltage  $v_G(t) = V_G + v_g \sin(2\pi ft)$ . As a result of this decrement of modulus and oscillation in the phase profile, both real and imaginary parts of  $y_{dg}$  tend to saturate at zero at very high frequencies after a dip around 1 GHz. It indicates that, at ultra-high frequencies, the transistor becomes completely unresponsive to the variations in  $v_g$ . However, as the operating frequency increases, the source partition of the channel charge does not suffer from the phase lag as drastically as compared to its drain counterpart. Yet, both real and imaginary parts of  $y_{sg}$  decreases monotonically with increasing frequency. Therefore, to balance the decrement of both  $y_{dg}$  and  $y_{sg}$ , the real and imaginary parts of  $y_{gg}$  increases with frequency in order to maintain  $y_{gg} + y_{dg} + y_{sg} = 0$ . The  $y_{gg}$  profile is depicted in Fig. 3(b). The  $\theta$ -dependence of  $y$ -parameters can be easily understood by recalling the  $\mu_e - \theta$  profile. As  $\mu_e$  is the largest along the armchair direction, the  $y_{dg}$  profile for  $\theta = 0^\circ$  tends to saturate at much higher frequencies compared to the same for  $\theta = 45^\circ$  or  $90^\circ$ . Conversely, the  $y_{dg}$  profile for  $\theta = 90^\circ$  saturates at the earliest with a lowest  $f_T$  of 0.16 GHz. However, the most interesting fact is that, the transcapacitances (for example,  $C_{dg}$ ) appear to be varying as a function of  $\theta$  only at high frequencies, whereas the transconductances ( $g_m$ , for example) are always  $\theta$ -dependent irrespective of the frequency of operation.

### F. Harmonic distortion analysis

We also conducted harmonic distortion analysis of the transistor at 0.25 GHz as illustrated in Fig. 3(c). Harmonic distortions arise from the inherent nonlinear character of the semiconductor devices. If a signal of fundamental frequency  $f_0$  is applied at the input, harmonics are observed in the output signal at integral multiples of  $f_0$  ( $2f_0$ ,  $3f_0$ , etc.) along with the fundamental frequency. To conduct the harmonic analysis, an input signal  $v_G(t) = V_G + v_g \sin(2\pi f_0 t)$  was applied at the gate terminal with  $f_0 = 0.25$  GHz, ensuring transistor saturation by  $V_G = V_D = 1$  V. The amplitude of the input sinusoid was chosen to be large enough ( $v_g = 0.1$  V) to produce nonlinear device behavior. Figure 3(c) depicts the output gate current spectra for both QS and NQS operations for  $\theta = 0^\circ$ . As shown, additional higher-order harmonics appear at 0.5 GHz ( $2f_0$ ) and 0.75 GHz ( $3f_0$ ) in the  $i_G$ -spectra for the NQS operation, whereas the QS model clearly underestimates these frequency components. This is because of the non-zero carrier inertia associated with the NQS model, which incurs phase shifts in the terminal currents at high frequencies.

### G. Effects of velocity saturation

To cater for the high- $f_T$  requirements of typical millimeter-wave applications, channel length scaling is necessary along with high bias voltages. However, in a small-channel-length device, the

carrier velocity tends to saturate due to the higher lateral electric field. Since such velocity saturation effect in any material can also be predicted by the first-principles-based approach;<sup>41</sup> here, we demonstrate how such phenomena can be added to our proposed “core” model.

Following the empirical Caughey–Thomas formalism,<sup>74</sup> the lateral electric field dependence of  $\mu_e$  can be modeled as

$$\mu_{eff} = \frac{\mu_e}{\left[1 + \left(\frac{\xi}{\xi_C}\right)^\sigma\right]^{1/\sigma}}, \quad (20)$$

where  $\mu_{eff}$  is the field-dependent mobility,  $\xi$  is the lateral electric field,  $\xi_C$  is the critical value of  $\xi$  for the velocity saturation, and  $\sigma$  is a fitting parameter. It is worth noting that  $\xi_C$  and  $\sigma$  are material specific parameters. By calibrating Eq. (20) with the results reported in Ref. 41 (see Fig. S6 of the [supplementary material](#)), numeric values of  $\xi_C$  were obtained as 30 MV/m with  $\sigma = 1$  for  $\theta = 0^\circ$  and 25 MV/m with  $\sigma = 2.5$  for  $\theta = 90^\circ$ . To incorporate the velocity saturation effect in our drain current model [Eq. (11)], we simply use Eq. (20) in the place of constant mobility  $\mu_e$  and replace  $\xi$  with  $(\psi_{SL} - \psi_{S0})/L$ . This approach is similar to BSIM3,<sup>75</sup> where  $(\psi_{SL} - \psi_{S0}) \approx V_D$  for low drain biases. However, it does not require any empirical parameter based artificial clamping of  $V_D$  at higher values. Although for a specific material (i.e., for a specific  $\sigma$ ), it might be possible to develop more rigorous yet semiempirical models for velocity saturation,<sup>76</sup> the proposed method captures the basic physics and is generalized for any arbitrary  $\sigma$ .

Figures 4(a) and 4(b), respectively, depict the variations of the maximum DC drain current ( $I_{DC,max}$ ) and associated  $f_T$  (at  $V_G = V_D = 1$  V) as functions of the channel length along armchair and zigzag directions. From Fig. 4(a), it is clear that the effect of velocity saturation is more pronounced along  $\theta = 0^\circ$  as compared to the zigzag direction due to the difference in  $\sigma$  values. We observe a similar effect in the  $f_T$  profile, varying as proportional to

$1/L^2$ . However, as obvious it is, due to channel length reduction,  $f_T$  was found to be as high as  $\sim 90$  GHz for  $L = 50$  nm along the armchair direction. For  $L = 50$  nm, Fig. 4(c) compares between the  $y_{dg}$  profiles, obtained both in the presence and absence of the velocity saturation. Clearly, as an effect of reduction in  $I_{DC}$  due to mobility degradation, the transconductance, i.e., the real part of  $y_{dg}$  also decreases leaving the imaginary part to remain almost unaltered. However, due to a higher value of  $\sigma$ , this effect is subdued along the zigzag direction. Nevertheless, due to high  $f_T$  values at  $L = 50$  nm,  $y_{dg}$  profiles tend to saturate at much higher frequencies. Since our model is based on the gradual channel approximation where the effect of lateral electric field in the electrostatics was completely ignored, we did not extend the results below 40 nm channel length where drain-induced barrier lowering and channel length modulation effects could be significant.

### H. RTA based approach and SPICE implementation

The presence of the  $\partial D_e(t)/\partial t$  term hinders the implementation of our CE based NQS model in a circuit simulator. Therefore, an RTA based approximate model was deduced from the CE based model in order to enable its implementation in SPICE (simulation program for integrated circuit emphasis)<sup>77</sup> using its Verilog–AMS interface. We develop the RTA model by defining NQS terminal charges in terms of their QS counterparts as per the following phenomenological equation:<sup>47</sup>

$$\frac{dQ_{T,NQS}}{dt} = -\frac{Q_{T,NQS} - Q_{T,QS}}{\tau}, \quad (21)$$

where  $\tau$  is the carrier relaxation time, re-defined with bias-dependent diffusivity as

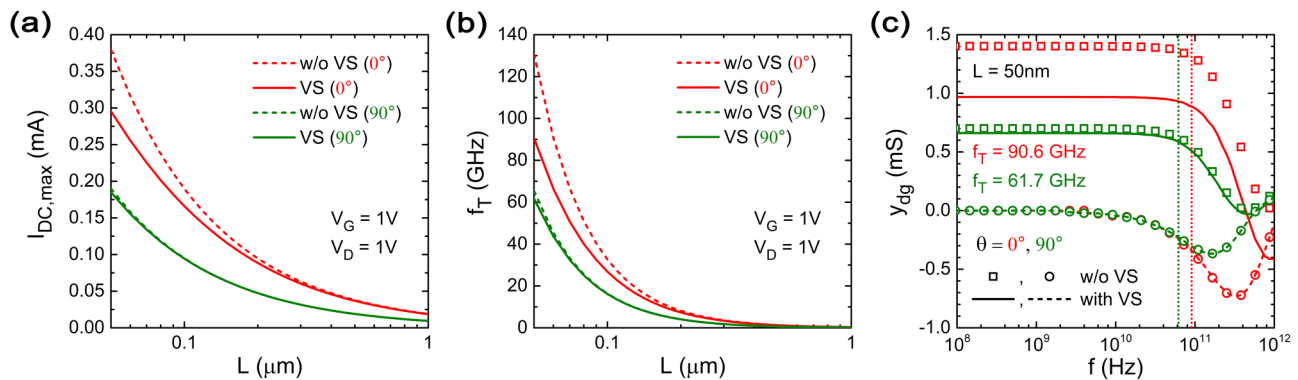


**FIG. 4.** (a) and (b), respectively, illustrate the variations of the maximum DC drain current and the intrinsic cut-off frequency as functions of the channel length for  $\theta = 0^\circ$  and  $90^\circ$ . For both (a) and (b), the transistor is biased at saturation with  $V_G = V_D = 1$  V. (a) demonstrates that the drain current for  $\theta = 0^\circ$  decreases as an effect of velocity saturation, whereas the current along the zigzag direction is less affected due to a higher value of  $\sigma$ . Similar observations can be made from (b). In (c), the small-signal parameter  $y_{dg}$  is plotted as a function of frequency both in the presence and absence of velocity saturation considering 50 nm channel length. Here, the symbols and lines, respectively, represent the results obtained in the absence and presence of the velocity saturation. As cut-off frequency gets increased due to a shorter channel length, both real and imaginary parts of  $y_{dg}$  tend to saturate at much higher frequencies.

$$\tau = \left[ \left( \frac{L^2 \kappa_{diff}}{D_e} \right)^{-1} + \left( \frac{|Q_I| \kappa_{drift}}{I_{DC}} \right)^{-1} \right]^{-1}. \quad (22)$$

In Eq. (22),  $Q_I = -Q_{G, QS}$  and the semi-empirical parameters  $\kappa_{diff}$  and  $\kappa_{drift}$  are, respectively, attributed to the diffusion and drift components of  $\tau$ . For phosphorene,  $\kappa_{diff} = \kappa_{drift} = 0.2$  (for all  $\theta$ ) was found to deliver a good match with the CE model up to  $2f_T$  as shown in Fig. 5(a). However, at higher frequencies ( $f > 2f_T$ ) or for very fast transients, the RTA approximation fails vigorously. After implementing the RTA based model in the SPICE simulator, we conducted transient and small-signal analysis of a resistive-load inverter and a common-source amplifier circuit. The schematics of the circuits are depicted in Fig. 5(b). In order to demonstrate the NQS effects in a digital circuit, the transient operation of the resistive-load inverter with supply voltage  $V_{DD} = 1$  V, load resistance  $R_D = 100$  k $\Omega$ , and load capacitance  $C_L = 40$  fF was simulated

under an ideal gate pulse of 50 ns time period. The result, as shown in Fig. 5(c), reveals that the QS model predicts some unphysical overshoots and undershoots in the output voltage waveform that surpasses even the input signal levels. However, this unphysical behavior is clearly eliminated by the NQS model. On the other hand, the gain-frequency characteristics of the common-source amplifier is demonstrated in Fig. 5(d) for  $\theta = 0^\circ, 45^\circ$ , and  $90^\circ$ . The saturation bias of the transistor was ensured by  $V_G = 0.75$  V,  $V_{DD} = 1$  V, and  $R_D = 0.08$  M $\Omega$ . A small sinusoidal signal of 1 mV amplitude with frequency varying from 1 Hz to 10 GHz is applied to the gate terminal, and the load resistance  $R_L$  was selected to be as high as 10 M $\Omega$  in order to obtain a nearly open-circuit voltage gain. Figure 5(d) illustrates that, while the low frequency gain (voltage gain  $A_V$ ) falloff, dictated by the DC blocking capacitance ( $C_{dc} = 100$  pF), is correctly captured by both QS and NQS models; the QS model, however, fails to correctly address the high frequency response. As illustrated in the figure, the QS model predicts  $|A_V|$  to diverge with increasing frequency, whereas the NQS model

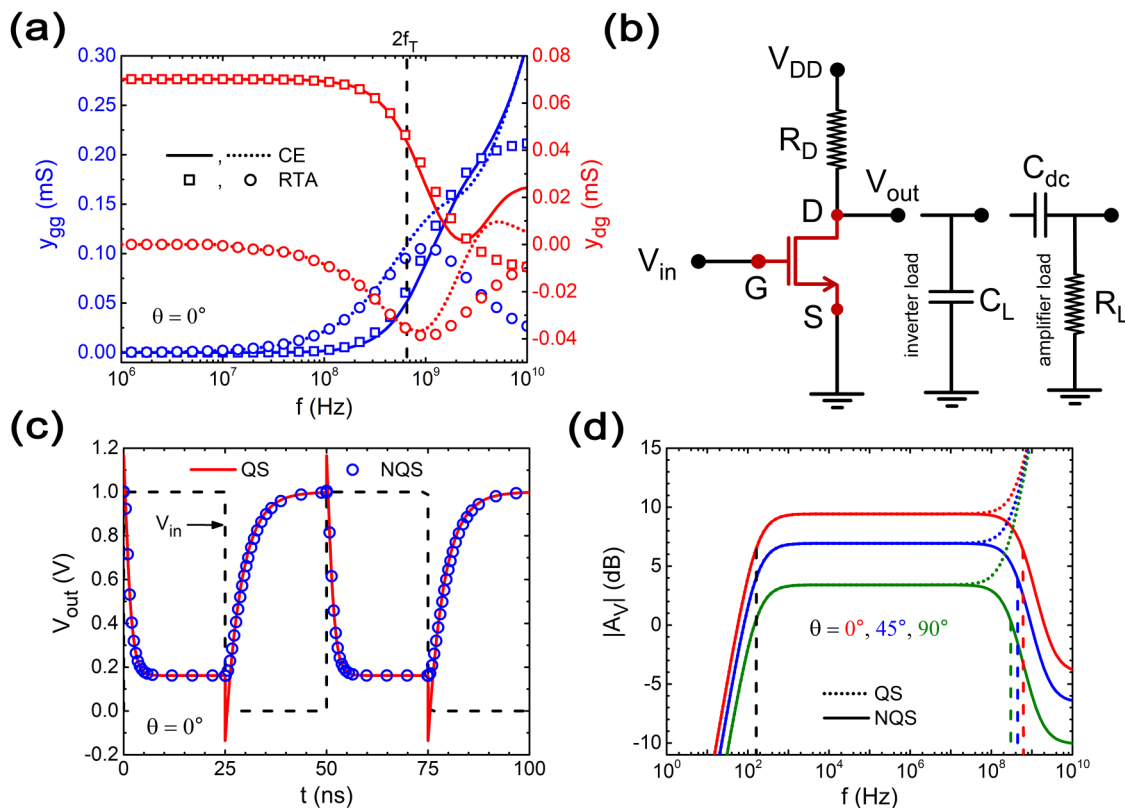


**FIG. 5.** (a) represents a match between the CE based model and the RTA based approach for  $\theta = 0^\circ$ . It shows that the RTA approximation holds good up to frequency  $2f_T$  that enables implementation of the NQS model in SPICE platform. (b) depicts the basic common-source configuration of the phosphorene transistor with inverter and amplifier loads. Static and dynamic simulations of the resistive-load inverter were carried out, and the output voltage waveform for an ideal pulse input is shown in (c) for  $\theta = 0^\circ$ . Unphysical spikes in the output voltage indicate the failure of the QS model for fast transients. Gain-frequency profiles of the common-source amplifier circuit are plotted in (d) for  $\theta = 0^\circ, 45^\circ$  and  $90^\circ$ . Maximum mobility along the armchair direction yields a maximum voltage gain for  $\theta = 0^\circ$ . It shows that while the gain response at high frequencies is correctly captured by the NQS model, the QS approximation on the contrary, assumes a divergent gain profile. (d) also indicates that the lower 3-dB cut-off frequency is constant for all  $\theta$  because it is determined by the DC blocking capacitor, whereas the higher 3-dB cut-off frequency varies with  $\theta$  due to different trans-capacitance values.

correctly characterizes the high frequency roll-off by defining a 3-dB cut-off frequency as dictated by the junction capacitances of the transistor. Nevertheless, the gain response and 3-dB bandwidths of the amplifier circuits for different  $\theta$  differ from each other due to the anisotropic mobility profile of phosphorene. These simulations clearly exemplify the importance of NQS models which helps one to recover a significant amount of the design space.

### III. CONCLUSIONS

Considering phosphorene as a prototypical example, we propose a first-principles-based device model that enables the prediction of channel-orientation-dependent high frequency performance of 2D transistor-based integrated circuits by considering the inertia of the charge carriers. The prediction can be made solely from the knowledge of the 2D material's crystal structure and thus it could be extremely useful for advanced technology research, where experimental data is scarce. Since most of these materials inherit low carrier mobilities, our model helps the circuit designer to extract maximum operating frequency from a transistor, which is very crucial for 2D material-based CMOS technology extension. On the other hand, the proposed model, which has been conceived as "core" in nature, facilitates inclusion of various non-ideal and short channel effects using standard pre-correction techniques for further development of the full-fledged industry-standard compact model as the technology matures. In a nutshell, the flexibility and widespread applicability of the proposed modeling framework significantly upgrades the designer's toolbox for the exploration of 2D material-based integrated circuits.

### IV. METHODS

#### A. Density functional theory calculations

First-principles calculations for free-standing monolayer phosphorene were carried out using the DFT code as implemented in QuantumATK<sup>78</sup> in conjunction with the generalized gradient approximation (GGA) exchange correlation and Perdew–Burke–Ernzerhof (PBE) functional.<sup>79</sup> The SG15<sup>80,81</sup> norm conserving pseudopotentials, as implemented in the QuantumATK database, were employed along with the LCAO (linear combination of atomic orbitals) basis sets of "medium" accuracy. The fermion occupation method was chosen to be the gaussian smearing with an electron temperature of 1000 K. The Brillouin zone integration was performed using a  $6 \times 8 \times 1$  Monkhorst–Pack<sup>82</sup> k-point grid along with 90 Hartree density-mesh cut-off energy and 1250 Hartree reciprocal cut-off energy. For the self-consistent calculations, the Pulay mixer algorithm was used with a maximum of 200 iteration steps, and the fast Fourier transform (FFT) method was followed for the Poisson solver. A sufficient vacuum of about 15 Å was provided in the  $z$ -direction of the phosphorene unit cell in order to avoid spurious interactions between periodic images. The geometry optimization of the phosphorene unit cell was carried out using a LBFGS (limited-memory Broyden–Fletcher–Goldfarb–Shanno)<sup>83</sup> optimizer with a maximum stress error tolerance of  $0.001 \text{ eV/Å}^3$  and a force tolerance of  $0.01 \text{ eV/Å}$ . Apart from this, a stencil order of 5 was used for the calculation of effective masses along ( $\Gamma - X$ ) and ( $\Gamma - Y$ ) directions.

### SUPPLEMENTARY MATERIAL

See the [supplementary material](#) for additional electronic structures, device characteristics, parameter calibrations, detailed analytical methods, and supporting MATLAB codes.

### AUTHORS' CONTRIBUTIONS

B.D. performed the DFT calculations, developed the model, conducted SPICE simulations, and analyzed final results. S.M. conceived the problem statement and overall supervised the work. Both authors contributed to manuscript writing.

### ACKNOWLEDGMENTS

This work was supported by the Mathematical Research Impact Centric Support (MATRICS) scheme of Science and Engineering Research Board (SERB), Government of India, under Grant No. MTR/2019/000047. The authors declare no competing financial and non-financial interest.

### DATA AVAILABILITY

The data that support the findings of this study are available within the article and its supplementary material. Other relevant data are available from the corresponding author upon reasonable request.

### REFERENCES

- <sup>1</sup>B. Radisavljevic, A. Radenovic, J. Brivio, V. Giacometti, and A. Kis, "Single-layer MoS<sub>2</sub> transistors," *Nat. Nanotechnol.* **6**, 147–150 (2011).
- <sup>2</sup>IEEE, in *International Roadmap for Devices and Systems, IEEE 2020, Beyond CMOS* (IEEE, 2020). See <https://irds.ieee.org/editions/2020>.
- <sup>3</sup>H. Li, J.-K. Huang, Y. Shi, and L.-J. Li, "Toward the growth of high mobility 2D transition metal dichalcogenide semiconductors," *Adv. Mater. Interfaces* **6**, 1900220 (2019).
- <sup>4</sup>S. Fathipour *et al.*, "Exfoliated multilayer MoTe<sub>2</sub> field-effect transistors," *Appl. Phys. Lett.* **105**, 192101 (2014).
- <sup>5</sup>M. J. Mleczko *et al.*, "Contact engineering high-performance n-type MoTe<sub>2</sub> transistors," *Nano Lett.* **19**, 6352–6362 (2019).
- <sup>6</sup>D. Ovchinnikov, A. Allain, Y.-S. Huang, D. Dumcenco, and A. Kis, "Electrical transport properties of single-layer WS<sub>2</sub>," *ACS Nano* **8**, 8174–8181 (2014).
- <sup>7</sup>Y. Jeong *et al.*, "2D MoSe<sub>2</sub> transistor with polymer-brush/channel interface," *Adv. Mater. Interfaces* **5**, 1800812 (2018).
- <sup>8</sup>Z. Wang *et al.*, "The ambipolar transport behavior of WSe<sub>2</sub> transistors and its analogue circuits," *NPG Asia Mater.* **10**, 703–712 (2018).
- <sup>9</sup>X. Sun *et al.*, "Performance limit of monolayer WSe<sub>2</sub> transistors; significantly outperform their MoS<sub>2</sub> counterpart," *ACS Appl. Mater. Interfaces* **12**, 20633–20644 (2020).
- <sup>10</sup>W. L. Liu *et al.*, "Effect of aging-induced disorder on the quantum transport properties of few-layer WTe<sub>2</sub>," *2D Mater.* **4**, 011011 (2017).
- <sup>11</sup>J. Shim *et al.*, "Polarity control in a single transition metal dichalcogenide (TMD) transistor for homogeneous complementary logic circuits," *Nanoscale* **11**, 12871–12877 (2019).
- <sup>12</sup>W. Zhu *et al.*, "Black phosphorus flexible thin film transistors at gigahertz frequencies," *Nano Lett.* **16**, 2301–2306 (2016).
- <sup>13</sup>H. Wang *et al.*, "Black phosphorus radio-frequency transistors," *Nano Lett.* **14**, 6424–6429 (2014).
- <sup>14</sup>C. Li *et al.*, "Black phosphorus high-frequency transistors with local contact bias," *ACS Nano* **14**, 2118–2125 (2020).

- <sup>15</sup>Y. Du, H. Liu, Y. Deng, and P. D. Ye, "Device perspective for black phosphorus field-effect transistors: Contact resistance, ambipolar behavior, and scaling," *ACS Nano* **8**, 10035–10042 (2014).
- <sup>16</sup>Y. Wang, G. Qiu, R. Wang *et al.*, "Field-effect transistors made from solution-grown two-dimensional tellurene," *Nat. Electron.* **1**, 228–236 (2018).
- <sup>17</sup>S. Berweger *et al.*, "Imaging carrier inhomogeneities in ambipolar tellurene field effect transistors," *Nano Lett.* **19**, 1289–1294 (2019).
- <sup>18</sup>See <https://www.2dsemiconductors.com/> for "2Dsemiconductors, USA."
- <sup>19</sup>See [www.hqgraphene.com/index.php](http://www.hqgraphene.com/index.php) for "HQ Graphene, the Netherlands."
- <sup>20</sup>N. Mounet *et al.*, "Two-dimensional materials from high-throughput computational exfoliation of experimentally known compounds," *Nat. Nanotechnol.* **13**, 246–252 (2018).
- <sup>21</sup>S. Haastrup *et al.*, "The computational 2D materials database: High-throughput modeling and discovery of atomically thin crystals," *2D Mater.* **5**, 042002 (2018).
- <sup>22</sup>J. Zhou *et al.*, "2DMatPedia, an open computational database of two-dimensional materials from top-down and bottom-up approaches," *Sci. Data* **6**, 86 (2019).
- <sup>23</sup>B. Das and S. Mahapatra, "An atom-to-circuit modeling approach to all-2D metal–insulator–semiconductor field-effect transistors," *NPJ 2D Mater. Appl.* **2**, 28 (2018).
- <sup>24</sup>E. G. Marin, M. Perucchini, D. Marian, G. Iannaccone, and G. Fiori, "Modeling of electron devices based on 2-D materials," *IEEE Trans. Electron Devices* **65**, 4167–4179 (2018).
- <sup>25</sup>B. Radisavljevic, M. B. Whitwick, and A. Kis, "Integrated circuits and logic operations based on single-layer MoS<sub>2</sub>," *ACS Nano* **5**, 9934–9938 (2011).
- <sup>26</sup>S. Wachter, D. K. Polyushkin, O. Bethge *et al.*, "A microprocessor based on a two-dimensional semiconductor," *Nat. Commun.* **8**, 14948 (2017).
- <sup>27</sup>Q. Gao, Z. Zhang, X. Xu *et al.*, "Scalable high performance radio frequency electronics based on large domain bilayer MoS<sub>2</sub>," *Nat. Commun.* **9**, 4778 (2018).
- <sup>28</sup>D. K. Polyushkin, S. Wachter, L. Mennel *et al.*, "Analogue two-dimensional semiconductor electronics," *Nat. Electron.* **3**, 486–491 (2020).
- <sup>29</sup>D. Yin, A. AlMutairi, and Y. Yoon, "Assessment of high-frequency performance limit of black phosphorus field-effect transistors," *IEEE Trans. Electron Devices* **64**, 2984–2991 (2017).
- <sup>30</sup>G. I. Zebrev, A. A. Tseluykovskiy, D. K. Batmanova, and E. V. Melnik, "Small-signal capacitance and current parameter modeling in large-scale high-frequency graphene field-effect transistors," *IEEE Trans. Electron Devices* **60**, 1799–1806 (2013).
- <sup>31</sup>J. G. Champlain, "A physics-based, small-signal model for graphene field effect transistors," *Solid-State Electron.* **67**, 53–62 (2012).
- <sup>32</sup>J.-D. Aguirre-Morales *et al.*, "A large-signal monolayer graphene field-effect transistor compact model for RF-circuit applications," *IEEE Trans. Electron Devices* **64**, 4302–4309 (2017).
- <sup>33</sup>D. Jiménez and O. Moldovan, "Explicit drain-current model of graphene field-effect transistors targeting analog and radio-frequency applications," *IEEE Trans. Electron Devices* **58**, 4049–4052 (2011).
- <sup>34</sup>X. Zheng, A. Calò, E. Albisetti *et al.*, "Patterning metal contacts on monolayer MoS<sub>2</sub> with vanishing Schottky barriers using thermal nanolithography," *Nat. Electron.* **2**, 17–25 (2019).
- <sup>35</sup>A. Allain, J. Kang, K. Banerjee, and A. Kis, "Electrical contacts to two dimensional semiconductors," *Nat. Mater.* **14**, 1195–1205 (2015).
- <sup>36</sup>Y. Xu *et al.*, "Contacts between two- and three-dimensional materials: Ohmic, Schottky, and p–n heterojunctions," *ACS Nano* **10**, 4895–4919 (2016).
- <sup>37</sup>L. Cheng, C. Zhang, and Y. Liu, "Why two-dimensional semiconductors generally have low electron mobility," *Phys. Rev. Lett.* **125**, 177701 (2020).
- <sup>38</sup>L. Li, Y. Yu, G. J. Ye *et al.*, "Black phosphorus field-effect transistors," *Nat. Nanotechnol.* **9**, 372–377 (2014).
- <sup>39</sup>J. Qiao, X. Kong, Z.-X. Hu *et al.*, "High-mobility transport anisotropy and linear dichroism in few-layer black phosphorus," *Nat. Commun.* **5**, 4475 (2014).
- <sup>40</sup>Y. Cao *et al.*, "Quality heterostructures from two-dimensional crystals unstable in air by their assembly in inert atmosphere," *Nano Lett.* **15**, 4914–4921 (2015).
- <sup>41</sup>G. Gaddemane *et al.*, "Theoretical studies of electronic transport in monolayer and bilayer phosphorene: A critical overview," *Phys. Rev. B* **98**, 115416 (2018).
- <sup>42</sup>G. I. Zebrev and R. G. Useinov, "Simple model of current-voltage characteristics of a metal–insulator–semiconductor transistor," *Fiz. Tekhn. Polupr. (Sov. Phys. Semicond.)* **24**, 777–781 (1990).
- <sup>43</sup>Y. Tsividis and C. McAndrew, *Operation and Modeling of the MOS Transistor*, 3rd edn (Oxford University Press, New York, 2011).
- <sup>44</sup>F. Pasadas and D. Jiménez, "Non-quasi-static effects in graphene field-effect transistors under high-frequency operation," *IEEE Trans. Electron Devices* **67**, 2188–2196 (2020).
- <sup>45</sup>E. G. Marin, S. J. Bader, and D. Jena, "A new holistic model of 2-D semiconductor FETs," *IEEE Trans. Electron Devices* **65**, 1239–1245 (2018).
- <sup>46</sup>W. Cao, J. Kang, W. Liu, and K. Banerjee, "A compact current-voltage model for 2D semiconductor based field-effect transistors considering interface traps, mobility degradation, and inefficient doping effect," *IEEE Trans. Electron Devices* **61**, 4282–4290 (2014).
- <sup>47</sup>D. Navarro *et al.*, "A carrier-transit-delay-based nonquasi-static MOSFET model for circuit simulation and its application to harmonic distortion analysis," *IEEE Trans. Electron Devices* **53**, 2025–2034 (2006).
- <sup>48</sup>Z. Zhu, G. Gildenblat, C. C. McAndrew, and I.-S. Lim, "Accurate RTA-based nonquasi-static MOSFET model for RF and mixed-signal simulations," *IEEE Trans. Electron Devices* **59**, 1236–1244 (2012).
- <sup>49</sup>Z. Jin, J. T. Mullen, and K. W. Kim, "Highly anisotropic electronic transport properties of monolayer and bilayer phosphorene from first principles," *Appl. Phys. Lett.* **109**, 053108 (2016).
- <sup>50</sup>Y. Trushkov and V. Perebeinos, "Phonon-limited carrier mobility in monolayer black phosphorus," *Phys. Rev. B* **95**, 075436 (2017).
- <sup>51</sup>M. Brahma, A. Kabiraj, M. Bescond, and S. Mahapatra, "Phonon limited anisotropic quantum transport in phosphorene field effect transistors," *J. Appl. Phys.* **126**, 114502 (2019).
- <sup>52</sup>A. S. Rodin, A. Carvalho, and A. H. Castro Neto, "Strain-induced gap modification in black phosphorus," *Phys. Rev. Lett.* **112**, 176801 (2014).
- <sup>53</sup>H. Liu *et al.*, "Phosphorene: An unexplored 2D semiconductor with a high hole mobility," *ACS Nano* **8**, 4033–4041 (2014).
- <sup>54</sup>L. Wang, A. Kutana, X. Zou, and B. I. Yakobson, "Electro-mechanical anisotropy of phosphorene," *Nanoscale* **7**, 9746–9751 (2015).
- <sup>55</sup>M. Yang *et al.*, "High performance CMOS fabricated on hybrid substrate with different crystal orientations," in *IEEE International Electron Devices Meeting 2003, Washington, DC, USA (IEEE, 2003)*, pp. 18.7.1–18.7.4.
- <sup>56</sup>A. N. Rudenko, S. Brener, and M. I. Katsnelson, "Intrinsic charge carrier mobility in single-layer black phosphorus," *Phys. Rev. Lett.* **116**, 246401 (2016).
- <sup>57</sup>G. Gildenblat, *Compact Modeling—Principles, Techniques and Applications* (Springer, Berlin, 2010).
- <sup>58</sup>M. M.- Mattausch, H. J. Mattausch, and T. Ezaki, *The Physics and Modeling of MOSFETs—Surface-Potential Model HiSIM* (World Scientific, Singapore, 2008).
- <sup>59</sup>S. V. Suryavanshi and E. Pop, "S2DS: Physics-based compact model for circuit simulation of two-dimensional semiconductor devices including non-idealities," *J. Appl. Phys.* **120**, 224503 (2016).
- <sup>60</sup>C. Herring and E. Vogt, "Transport and deformation-potential theory for many-valley semiconductors with anisotropic scattering," *Phys. Rev.* **101**, 944–961 (1956).
- <sup>61</sup>D. Xiang, C. Han, J. Wu *et al.*, "Surface transfer doping induced effective modulation on ambipolar characteristics of few-layer black phosphorus," *Nat. Commun.* **6**, 6485 (2015).
- <sup>62</sup>N. Sharan and S. Mahapatra, "Nonquasi-static charge model for common double-gate MOSFETs adapted to gate oxide thickness asymmetry," *IEEE Trans. Electron Devices* **60**, 2419–2422 (2013).
- <sup>63</sup>S.-Y. Oh, D. E. Ward, and R. W. Dutton, "Transient analysis of MOS transistors," *IEEE Trans. Electron Devices* **27**, 1571–1578 (1980).

- <sup>64</sup>T. Smedes and F. M. Klaassen, “An analytical model for the non-quasi-static small-signal behaviour of submicron MOSFETs,” *Solid-State Electron.* **38**, 121–130 (1995).
- <sup>65</sup>S. Sarkar, A. S. Roy, and S. Mahapatra, “Unified large and small signal non-quasi-static model for long channel symmetric DG MOSFET,” *Solid-State Electron.* **54**, 1421–1429 (2010).
- <sup>66</sup>H. Wang, T.-L. Chen, and G. Gildenblat, “Quasi-static and nonquasi-static compact MOSFET models based on symmetric linearization of the bulk and inversion charges,” *IEEE Trans. Electron Devices* **50**, 2262–2272 (2003).
- <sup>67</sup>A. S. Roy, J. M. Vasi, and M. B. Patil, “A new approach to model nonquasi-static (NQS) effects for MOSFETs—Part I: Large-signal analysis,” *IEEE Trans. Electron Devices* **50**, 2393–2400 (2003).
- <sup>68</sup>A. S. Roy, J. M. Vasi, and M. B. Patil, “A new approach to model nonquasi-static (NQS) effects for MOSFETs—Part II: Small-signal analysis,” *IEEE Trans. Electron Devices* **50**, 2401–2407 (2003).
- <sup>69</sup>A. S. Roy, C. C. Enz, and J.-M. Sallese, “Compact modeling of anomalous high-frequency behavior of MOSFET’s small-signal NQS parameters in presence of velocity saturation,” *IEEE Trans. Electron Devices* **53**, 2044–2050 (2006).
- <sup>70</sup>C. Turchetti, P. Mancini, and G. Masetti, “A CAD-oriented nonquasistatic approach for the transient analysis of MOS IC’s,” *IEEE J. Solid-State Circuits* **21**, 827–836 (1986).
- <sup>71</sup>S. W. Hwang, T.-W. Yoon, D. H. Kwon, Y. S. Yu, and K. H. Kim, “A physics-based, SPICE (simulation program with integrated circuit emphasis)-compatible non-quasi-static MOS (metal-oxide-semiconductor) transient model based on the collocation method,” *Jpn. J. Appl. Phys.* **37**, L119–L121 (1998).
- <sup>72</sup>N. Sharan and S. Mahapatra, “Continuity equation based nonquasi-static charge model for independent double gate MOSFET,” *J. Comput. Electron.* **13**, 353–359 (2014).
- <sup>73</sup>F. Pasadas, E. G. Marin, A. Toral-Lopez *et al.*, “Large-signal model of 2DFETs: Compact modeling of terminal charges and intrinsic capacitances,” *NPJ 2D Mater. Appl.* **3**, 47 (2019).
- <sup>74</sup>D. M. Caughey and R. E. Thomas, “Carrier mobilities in silicon empirically related to doping and field,” *Proc. IEEE* **55**, 2192–2193 (1967).
- <sup>75</sup>Y. Cheng and C. Hu, *MOSFET Modeling & BSIM3 User’s Guide* (Kluwer Academic Publishers, 2002).
- <sup>76</sup>J. Cao *et al.*, “A new velocity saturation model of MoS<sub>2</sub> field-effect transistors,” *IEEE Electron Device Lett.* **39**, 893–896 (2018).
- <sup>77</sup>Silvaco Inc., *SmartSpice, Analog Circuit Simulator—Users’ Manual, Version 4.10.6.R* (Silvaco Inc., Santa Clara, CA, 2014). See <https://www.silvaco.com/>.
- <sup>78</sup>See <https://www.synopsys.com/silicon/quantumatk.html> for “QuantumATK with Virtual NanoLab, Synopsys, Denmark” (last accessed September 1, 2020).
- <sup>79</sup>J. P. Perdew, K. Burke, and M. Ernzerhof, “Generalized gradient approximation made simple,” *Phys. Rev. Lett.* **77**, 3865 (1996).
- <sup>80</sup>D. R. Hamann, “Optimized norm-conserving Vanderbilt pseudopotentials,” *Phys. Rev. B* **88**, 085117 (2013).
- <sup>81</sup>M. Schlipf and F. Gygi, “Optimization algorithm for the generation of ONCV pseudopotentials,” *Comput. Phys. Commun.* **196**, 36–44 (2015).
- <sup>82</sup>H. J. Monkhorst and J. D. Pack, “Special points for Brillouin-zone integrations,” *Phys. Rev. B* **13**, 5188 (1976).
- <sup>83</sup>D. C. Liu and J. Nocedal, “On the limited memory BFGS method for large scale optimization,” *Math. Program.* **45**, 503–528 (1989).